Modeling and Measurement of Residual Stresses in a Steel Vessel Containing Glass

AQ1

S. Nakhodchi[1]
Former Ph.D. Research Student
Department of Mechanical Engineering,
University of Bristol,
Bristol, UK

B. G. Thomas
Professor
Department of Mechanical and Industrial Engineering,
University of Illinois at Urbana-Champaign,
1206 West Green Street,
Urbana, IL 61801

D. J. Smith[2]
Professor
Department of Mechanical Engineering,
University of Bristol,
Queen's Building, University Walk,
Bristol BS8 1TR, United Kingdom
e-mail: david.smith@bristol.ac.uk

Residual stresses in a stainless steel vessel containing glass have been evaluated using measurements and numerical simulation. High-level nuclear wastes are often vitrified in glass cast in cylindrical stainless steel containers. Knowledge of the internal stresses generated in both the glass and container during this process is critical to structural integrity and public safety. In this research, residual stresses were measured near the surface of a High Level Waste container using an Incremental Center Hole Drilling technique. Residual stress magnitudes were found to be at or near to the yield stress in the container wall. A transient finite-element thermal-stress model has been developed to simulate temperature, distortion, and stress during casting and cooling in a simple slice domain of both the glass and the container. Contact thermal-stress elements were employed to prevent penetration at the glass–container interface. Roughness of these contact surfaces was modeled as an equivalent air gap with temperature-dependent conductivity in the thermal model. The stress model features elastic-viscoplastic constitutive equations developed based on the temperature-dependent viscosity of the glass and elastic-plastic constitutive equations for the stainless steel. The simulation was performed using the commercial ABAQUS program with a user material subroutine. The model predictions are consistent with the residual stress measurements, and the complete thermal–mechanical behavior of the system is evaluated. [DOI: 10.1115/1.4004157]

Keywords: thermal stress, residual stress, finite element, high-level waste, thermomechanical process, constitutive model

1 Introduction

Residual stress plays a significant role in the failure of engineering materials. They are an inevitable consequence of most manufacturing processes. Residual stresses can combine with the applied inservice load so may be either beneficial or detrimental. To predict and control their contribution, it is crucial to understand the source of the residual stresses [1–3].

Radioactive nuclear wastes have been produced in the UK since the 1940s. The main sources of these wastes are byproducts of the operation of power generation reactors for the production of electricity, nuclear-powered submarine program in UK, and use of nuclear material in industry and medicine [4]. These wastes are normally classified as low level waste, intermediate level waste, and high level waste (HLW). Low and intermediate level wastes comprise approximately 97% of the total volume of waste generated worldwide and contain only 5% of radioactivity, whereas high level wastes are just 3% of the total volume but hold 95% of the total radioactivity [5].

High level waste contains the waste products from reprocessing of spent nuclear fuels. These waste products arise in the form of highly radioactive nitric acid solutions, which are then introduced into borosilicate glass that is poured into stainless steel containers, using processes called vitrification and encapsulation, respectively [6,7]. The underlying reason behind this conversion is to provide a solid, stable, and durable material that can be more easily stored or transported than the original wastes. Waste is temporarily stored at the solidification processing plant, during which time the heat generated by the decay of the fission products decreases. Although in the UK a long term plan is yet to be decided, permanent storage of these waste containers in an underground repository is the likely strategy [8].

The structural integrity of HLW containers has a significant role in the safety assessment of both temporary and permanent storage locations. Thus, in order to evaluate structural integrity of the HLW containers, quantitative understanding of the residual stress distributions and deformations in the final product of the vitrification process is necessary.

In the waste vitrification process, radioactive waste is captured in glass. Concentrated highly active liquor (HAL), arising from reprocessing operations, is converted into glass for safe interim storage in the vitrification product store. HAL, which is first stored in highly radioactive storage tanks, is transferred in batches to a liquid feed stock tank. It is metered into a rotating tube furnace, which converts it to an oxide powder in a semicontinuous operation. Then the calcined HAL is melted together with glass in a controlled temperature vessel at 1100 °C and the product is cast into a stainless steel container. This vitrified product is usually poured at 1050 °C [9]. After pouring into the container, the system is allowed to cool and a lid is fitted. After further cooling, the lid is welded to the container. Following the welding process, the container surface is swabbed and monitored for surface radioactivity, in order to ensure safe transfer of the container to the storage facility.

Previous work in this area has been confined to internal programmes within sponsoring companies and little information is provided in the open literature. For example, work by Pennick [10] within BNFL (a predecessor to Nexia) examined the development of residual stresses during the cooling of glass in waste containers. In this paper, experiments and analysis are performed to simulate this process using glass to represent HLW, and residual stress measurements are made on the full-scale stainless steel container. A transient finite-element model is then developed and

applied to simulate the thermal–mechanical behavior of a representative slice through both the solidifying glass and the stainless steel container. The model explains how the measured residual stresses develop and together the results reveal consistent new insights into this important waste-disposal process.

2   Glass Pouring Experiments

Experiments were performed by the National Nuclear Laboratory (NNL) (previously Nexia Solutions Limited) to pour glass, used to simulate radioactive waste, into a Type 309 stainless steel container. The dimensions of the stainless steel container are shown in Fig. 1.

The wall thickness of the container was 5 mm with an external diameter of 430 mm. The container was first preheated to 600 °C. Then molten glass with an initial temperature of 1050 °C was poured into the warm container in two stages. Figure 2(a) shows the location of the thermocouples attached to the stainless steel container and were located at three positions down the surface of the stainless steel cylinder. Figure 2(b) shows the surface temperature histories measured by each thermocouple during the process. They clearly indicate a peak temperature of about 800 °C in the outer wall in the first fill and a similar peak temperature after

Fig. 1   Dimensions of stainless steel container (in mm)

about 8 h for the second fill. After the second fill, the filled container is allowed to cool over a period of 40 h. These data are used later in the finite-element simulations to guide the development of the model.

3   Residual Stress Measurement Method

Earlier residual stress measurements were undertaken by Pennick [10] as part of internal work at BNFL (a predecessor company to Nexia). He reported stress measurements in a full-scale container during filling operations using high temperature weldable strain gauges and laser speckle photography. Residual stresses were then measured using strain gauges via an air abrasive technique. The strain gauges showed great fluctuations during the filling and stresses increased during the cooling process.

In the current project, the incremental center hole drilling (ICHD) method was used to measure residual stresses near to the surface of the stainless steel container only. The ICHD method is a semidestructive stress-relief technique that measures residual strains close to the surface of a component during the drilling of a shallow, blind hole. An inverse method is then used to determine three components of released surface strain, which are finally converted to residual stress components. The ICHD method has been applied extensively to metals [11–14], nonmetals [15], and composite materials [16,17]. The ICHD technique is a refinement of the center hole drilling method to measure nonuniform stress profiles [18–21]. In the ICHD technique, the calibration coefficients should be obtained prior to measurement, using experiments or the finite-element method [20,22]. Among different data analysis procedures [21,23], the integral method [23,24] is the most common method for analyzing the data obtained from the experiment. Recent developments of the ICHD method can be found in Ref. [25].

The ICHD technique was performed to measure surface residual stresses in the stainless steel container after it had completely cooled. Measurements were carried out at three locations at the middle section of the container at intervals of 120° around the circumferential of the container. This is shown schematically in Fig. 3(a). Strain gauge rosettes with an external diameter of 5.13 mm corresponding to type 062UL were used to measure the released surface strains after each step of drilling. Figure 3(b) shows a schematic diagram of a typical three element strain gauge rosette [26]. A RS-200 precision milling guide was used combined with a 1.6 mm diameter specific purpose drill provided by Vishay Measurement Group for manufacturing the hole. The hole was drilled in incremental steps, as small as 0.016 mm close to the surface. Bigger increment sizes were chosen later.

Residual stresses were calculated from the measured surface strains using the integral method. In the integral method, residual strain and released residual stresses are related by

$$\varepsilon_r(h) = \frac{1+\nu}{2E}\int_0^h a(z,h)(\sigma_{\max}(z)+\sigma_{\min}(z))d_z$$
$$+ \frac{1}{2E}\int_0^h b(z,h)(\sigma_{\max}(z)-\sigma_{\min}(z))\cos 2\beta(z)dz \quad (1)$$

where E is the Young modulus, ν is the Poisson ratio, $a(z,h)$ and $b(z,h)$ are calibration coefficients in a depth of z for a hole with the depth of h, $\sigma_{\max}(z)$ and $\sigma_{\min}(z)$ are the maximum and minimum principal stresses at the depth z. By considering a uniform stress distribution over an increment, Eq. (1) can be rewritten in the form

$$\varepsilon_{xn} = \frac{1}{2E}\sum_{i=1}^n \left[(1+\nu)a_{ni}(\sigma_{xi}+\sigma_{yi})+b_{ni}(\sigma_{xi}-\sigma_{yi})\right]n = 1...N$$
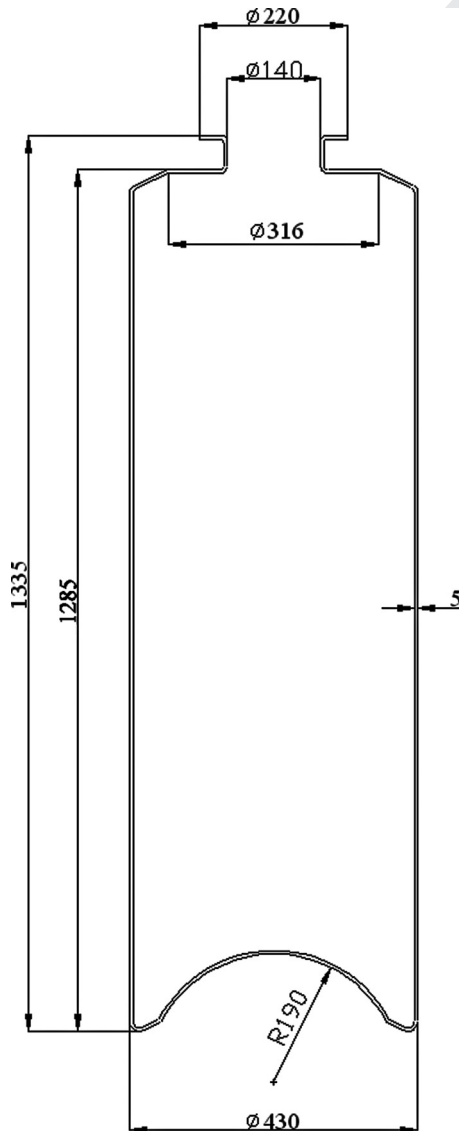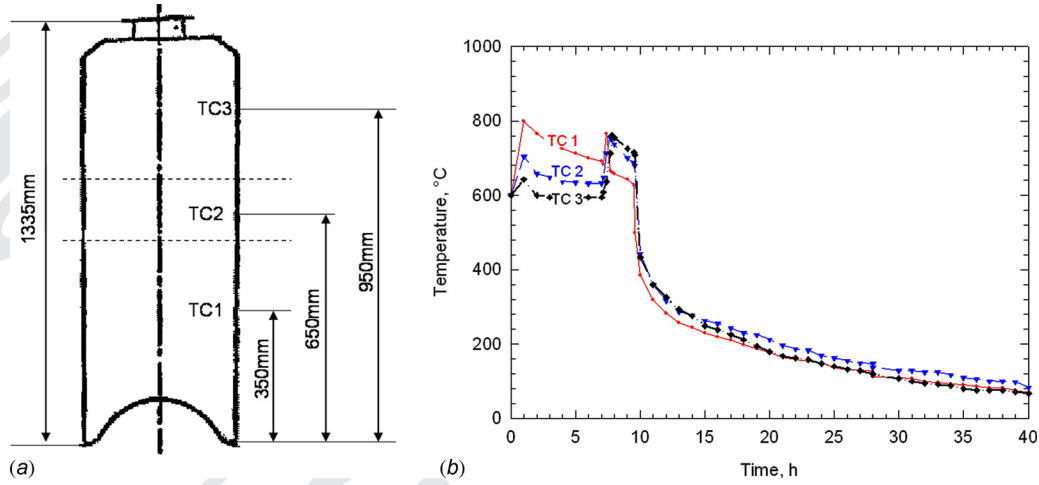
$$(2)$$

Fig. 2 (*a*) **Location of thermocouples on the steel container and** (*b*) **time-temperature histories measured during filling of the container**

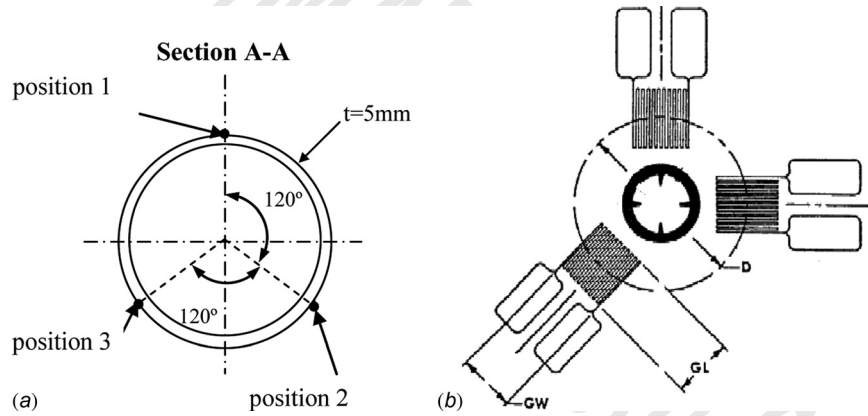**Fig. 3** (*a*) **Locations of the ICHD measurements on the stainless steel container and** (*b*) **schematic diagram of a typical three element strain gauge rosette [26]**

where n is the depth increment, σ_{xi} and σ_{yi} are stresses equivalent to the uniform residual stress within the ith layer and a_{ni}, b_{ni} are the calibration coefficient provided by the finite-element analysis [21].

The residual strains and stresses can be written in the form

$$p_n = \frac{\varepsilon_{1n} + \varepsilon_{2n}}{2}, \quad q_n = \frac{\varepsilon_{1n} - \varepsilon_{2n}}{2}, \quad t_n = \frac{\varepsilon_{1n} - 2\varepsilon_{2n} + \varepsilon_{3n}}{2} \quad (3)$$

$$P_n = \frac{\sigma_x + \sigma_y}{2}, \quad Q_n = \frac{\sigma_x - \sigma_y}{2}, \quad T_n = \frac{\sigma_x - 2\tau_{xy} + \sigma_y}{2} \quad (4)$$

where p_n, q_n, and t_n are strains and P_n, Q_n, and T_n are stresses calculated for each drilling step [24]. Equation (2) can be now solved and rewritten in matrix form as

$$\{P\} = \frac{E}{1+\nu}[A]^{-1}.\{p\}, \quad \{Q\} = E[B]^{-1}.\{q\}, \quad \{T\} = E[B]^{-1}.\{t\} \quad (5)$$

where $\{P\}, \{Q\}$, and $\{T\}$ are stress vectors, $\{p\}$, $\{q\}$, and $\{t\}$ are strain vectors. $[A]$ and $[B]$ are calibration coefficient matrices.

Finally, the principal stress and strain vectors, σ_{max} and σ_{min}, and their orientation,β, are calculated using

$$\sigma_{max}, \sigma_{min} = \{P\} \pm \sqrt{\{Q\}^2 + \{T\}^2} \quad (6)$$

$$\beta = \frac{1}{2}\arctan\left(\frac{\{T\}}{\{Q\}}\right)$$

The ICHD residual stress measurement experiments were carried out, and an inhouse MATLAB data analysis program [25], incorporating the above equations, was applied to compute the residual stresses. These are presented in Sec. 4.

AQ3

4   Residual Stress Measurement Results

Measured relaxed strains at position 1 on the circumference of the cylinder ((Fig. 3(*a*)) are shown in Fig. 4. Similar results were obtained from measurements at the 120 deg and 240 deg positions. The average of the residual stresses in the hoop and axial directions were determined from the computed stresses, and in Fig. 5, the profiles of the average of the stress components through the stainless steel container are illustrated.

With increasing depth beneath the surface, the inaccuracy of the measured stresses increases. This is due to the inherent limitation of the ICHD technique based on the St. Venant Principle, which indicates that the surface strains are mainly controlled by stresses close to that surface. This problem has been noted previously [22]. Therefore, calculated stresses are limited to measurement of up to the total depth of 0.7 mm below the surface. Tensile hoop stresses varied from 0 at the surface up to approximately 350 MPa at 0.7 mm below the surface. Similarly, axial stresses
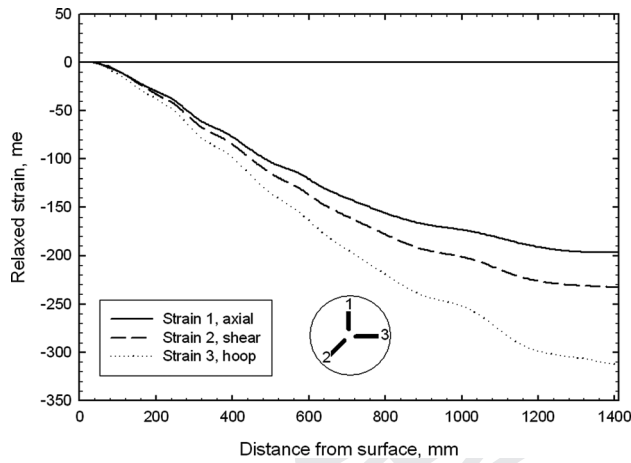
Fig. 4   Typical measured relaxed strains (in microstrain, position 1)
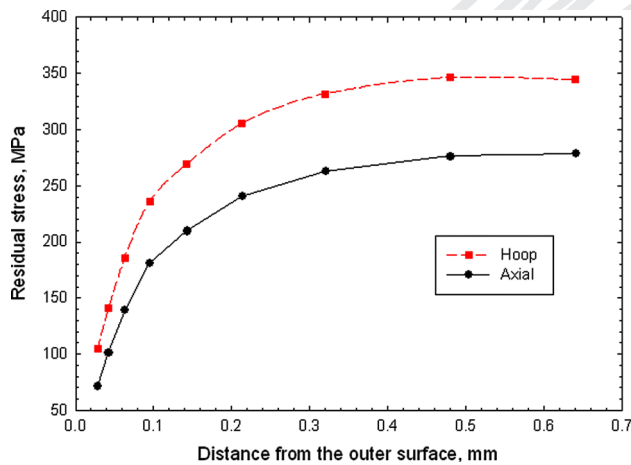

Fig. 5   Average measured hoop and axial residual stress

were tensile and vary from 0 to 400 MPa at 0.7 mm below the surface. The variation of the residual stresses from the surface to the interior reflects two features. First initial residual stresses arising from the initial manufacture of the cylinder maybe present. Although no measurements were made prior to filling, it is likely that if initial residual stresses were present they were relaxed by creep during the preheating phase prior to filling the cylinder. Second, there is evidence [25] to suggest that very near surface measurements are prone to significant error. This leads to the conclusion that the measurements over the depth 0.2–0.7 mm represent the residual stresses created during the filling process.

The yield stress of 309 stainless steel is reported to be between 297 and 353 MPa [27]. This indicates that the peak measured residual stresses were close to the yield stress. Although plasticity causes uncertainties in the results, the measured residual stresses exceed the expected values. Consequently, the measurements suggest that the maximum residual stresses were close or near to the yield stress.

To obtain a more complete understanding of the evolution of the stresses in both the stainless steel and the glass, a finite-element model was developed to simulate the process. This is explained in the following sections. Notably, the residual stresses were measured only in the containment vessel and not in the glass.

5   Finite-Element Model

Thermal–mechanical finite-element analysis was performed to provide a fundamental understanding of transient temperature evolution and the generation of stresses in the solidifying glass and the stainless steel container during this casting process. The model was developed at the University of Illinois, Urbana, IL, based on software and user material subroutines developed in previous work to simulate the continuous casting of steel [28–32].

Glass has an amorphous crystal structure that at room temperature is solid and brittle and hardly deforms plastically, exhibiting entirely elastic behavior [33]. At higher temperatures, most previous research on thermal stresses in glass have been confined to the study of an infinite plate with a uniform initial temperature, which is cooled either suddenly, via glass tempering, or gradually, via annealing. The initial temperature conventionally has been set to within the temperature range close to the glass transition temperature. The resulting residual stress has been shown to be approximately parabolic with tension in the middle of the cross section and compression at the edges [34,35].

Different models have been suggested for prediction of residual stresses in glass. A so-called "instant freezing" model assumed liquid glass converted to solid instantly [36]. This model was followed by development of viscoelastic behavior for glass in the transient temperature range [35,37]. Considering the viscous flow and variation of the viscosity by temperature, viscoplastic models have also been suggested for glass. These models for example have been used in simulation of glass sheet forming to predict the behavior of the glass sheet while cooling under its own weight [38–40]. A material model similar to the latter is employed for glass in this research.

The domain adopted for the finite-element simulations in this work is a thin radial slice through the entire geometry, taking advantage of the axisymmetric nature of the process. The slice considered is at the middle height of the container, as shown in Fig. 6(a). This is the same height as thermocouple TC2, Fig. 2. The model includes separate meshes (parts) for the glass and stainless steel so that boundary conditions between them can properly represent the thermal and physical interaction (intermittent contact) between the glass and the container. Since only a radial slice was used in the analysis, the ends of the cylinder were not included.

The model consists of separate thermal and mechanical analysis stages. As part of this work, a realistic elastic-viscoplastic constitutive model was developed to simulate mechanical behavior of the glass from the liquid to solid state.

5.1   Thermal Model Governing Equations. The heat transfer model solves the transient heat conduction equation, Eq. (7) for heat conservation along with the boundary conditions, Eqs. (8–10), to define the heat input to every portion of the domain boundary

$$\rho C_p \frac{\partial T}{\partial t} = \frac{\partial}{\partial x_i}(k_{\text{eff}}) \frac{\partial T}{\partial x_i} \tag{7}$$

where ρ is the density, Cp is the specific heat, and k_{eff} is the effective isotropic temperature dependant conductivity as shown in Fig. 8(b) and given in Table 1.

The boundary conditions can be expressed by

$$-k\frac{\partial T}{\partial x} = q \tag{8}$$

and are split into different regions, as shown in Fig. 6(b). A symmetry boundary condition is imposed at the top and bottom surfaces by assigning q = 0 at the glass central axis and by neglecting the small temperature gradient in the axial direction, z, as illustrated in Fig. 6(c). Within the glass, heat is transferred by conduction. Heat is lost from the exterior surface of the glass through conduction to the steel, across the glass–steel wall interface where thermal contact conductance between surfaces is considered. The glass is assumed not to wet the container because when it touches
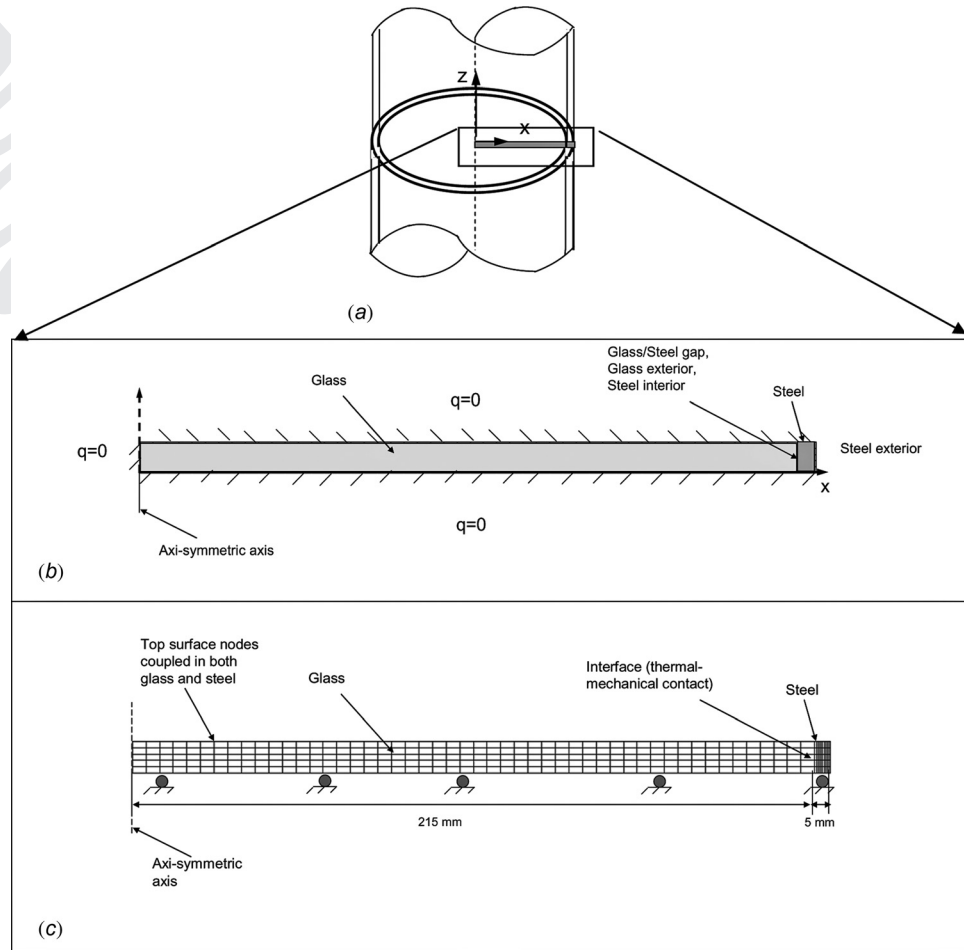
Fig. 6   (*a*) Finite-element domain, (*b*) mesh and thermal boundary conditions, and (*c*) structural boundary conditions
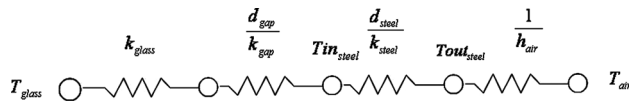

Fig. 7   Schematic heat resistance model used in the heat transfer model

the relatively cold walls, the glass stops flowing locally, owing to a rapid increase in its local viscosity.

Heat flux across the glass–steel interface is mathematically imposed by

$$q = \frac{k_{\mathrm{air}}}{d_{\mathrm{gap}}} (T_s - T_g) \tag{9}$$

where a gap of 0.1 mm represents the surface roughness of steel container, and the temperature-dependant thermal conductivity of air [41] is listed in Table 2.
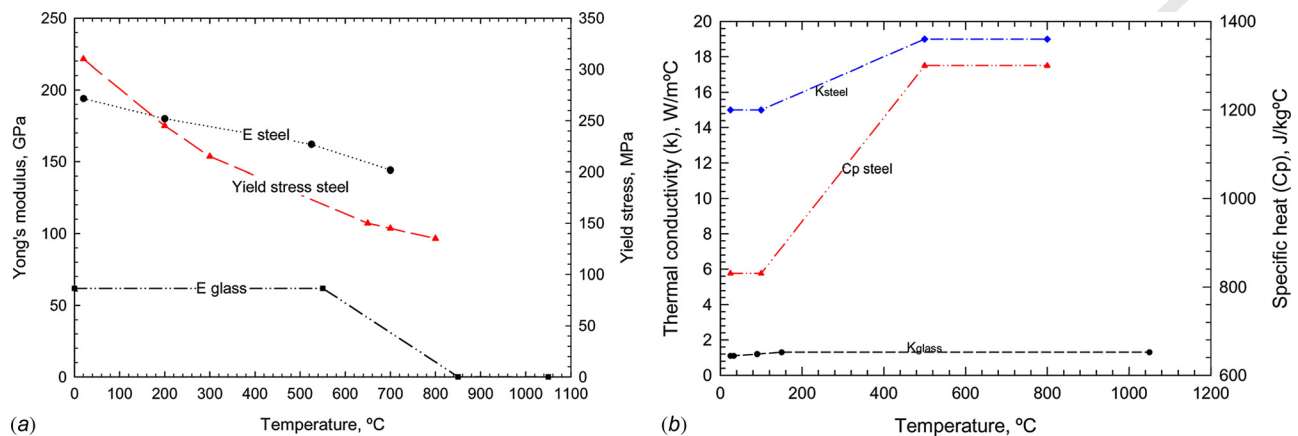
Fig. 8   Temperature dependant (*a*) mechanical and (*b*) thermal properties of stainless steel and glass

Table 1 Material property of glass and steel

Parameter	Value
E_{glass} (GPa) in solid state ($<525\ ^\circ$C)	62
E_{glass} (GPa) in liquid state ($>850\ ^\circ$C)	1
Density ρ (kg/m^3) in solid state	2400
Density ρ (kg/m^3) in liquid state	2200
Thermal expansion coefficient of glass (m/m)	3.2×10^{-6} and
assumed to vary linearly between 20 and 850 $^\circ$C[a]	5.0×10^{-6}
Specific heat of steel (J/kg$^\circ$C)	500

[a]Larger thermal expansion coefficients arise near to the set-point, where the glass is very fluid, soft, and unable to sustain any significant stress. These have not been included here.

Table 2 Conductivity of air with temperature [41]

Temperature ($^\circ$C)	Conductivity (W m^{-1} K^{-1})
200	0.032
400	0.039
600	0.045
800	0.051
1000	0.057
1200	0.063
1400	0.068

Some of this heat flux causes the steel wall to heat up and some heat conducts through the wall to be lost from the steel exterior by convection with the air at the ambient temperature given by

$$q = h_{air}(T_S - T_a) \tag{10}$$

Similar thermal boundary conditions have been previously implemented in simulations of static-cast steel ingots [42]. A schematic heat-resistor diagram shown in Fig. 7 describes the heat transfer and boundary conditions in the entire domain.

The initial temperature of the glass was set to 1050 $^\circ$C and initial temperature of 600 $^\circ$C was assigned to the elements represent the steel part. The optimum film coefficient of 10 W/m^2 $^\circ$C was found and applied to the exterior surface of glass such that the predicted temperature history on the stainless steel matched with the thermocouple reading obtained from experiment.

5.2 Mechanical Model Governing Equations. The mechanical analysis involves solving the equilibrium equations, constitutive equations, and compatibility equations, which relate force to stress, stress to strain, and strain to displacement, respectively [43]. In the Lagrangian frame appropriate for this work, the force equilibrium balance given in Eq. (11) is the general governing equation for the static-mechanics problem, where ρ is the density and σ_{ij} is the stress tensor.

$$\nabla \cdot \sigma_{ij} + \rho gh = 0 \tag{11}$$

where the second term represents the body force from the hydrostatic pressure due to gravity and h is the height of molten glass above the simulated slice. Inserting values for density, $\rho = 2200$ kg/m^3, gravity g $= 9.8$ m/s^2, h $= 0.65$ m, r $= 215$ mm, and Δr $= 5$ mm, the hoop stress σ_{hoop} due to hydrostatic pressure $\sigma_{hoop} = \rho ghr/\Delta r = 0.602$MPa which is negligible compared to the measured stresses and calculated thermal stresses discussed later. Thus, the difference between slices at different heights is negligible and so the assumption of a state of generalized plane-strain in a single slice is valid. The compatibility equations to relate strains and displacements are given by

$$\dot{\varepsilon} = \frac{d}{dt}\left[\frac{1}{2}\left(\nabla \boldsymbol{u} + (\nabla \boldsymbol{u})^T\right)\right] \tag{12}$$

where $\boldsymbol{u}$ is the displacement vector.

Different constitutive models were used for the steel and glass parts of the model. For grade 309 stainless steel container, linear isotropic hardening was assumed at 20 $^\circ$C and elastic perfectly plastic behavior at higher temperatures. The temperature-dependant Young's modulus used in this model was fitted to the experimental data provided by NNL [27] and is shown in Fig. 8(a) along with temperature dependent yield stress of stainless steel. A constant Poisson ratio of 0.3 was assumed.

In glass cooling, stress generation is a rate-dependent process, which can be treated as a transient solidification process phenomenon using a rate formation. Therefore, the total strain rate can be divided into three components of elastic strain rate, $\dot{\varepsilon}_{el}$, thermal strain rate, $\dot{\varepsilon}_{th}$, and inelastic strain rate, $\dot{\varepsilon}_{in}$, where

$$\dot{\varepsilon}_{total} = \dot{\varepsilon}_{el} + \dot{\varepsilon}_{th} + \dot{\varepsilon}_{in} \tag{13}$$

Elastic strain is directly responsible for stress. Equation (14) can be obtained by differentiating the classical elastic tensor equations relating stress and strain components for a linear material with negligible large rotations.

$$\dot{\sigma} = D : (\dot{\varepsilon}_{total} - \dot{\varepsilon}_{th} - \dot{\varepsilon}_{in}) \tag{14}$$

where D is the fourth-order tensor of elastic constants, characterized here for an isotropic material by the temperature-dependent elastic modulus, given in Table 1 and shown in Fig 8(a), and a constant Poisson ratio, 0.2.

5.2.1 Thermal Strain. Thermal strains are found from the temperature field calculated by the heat transfer model. They arise due to volume changes caused by temperature differences

$$\varepsilon_{th} = \int_{T0}^{T} \alpha(T)dT \tag{15}$$

where α is the average coefficient of thermal expansion between the reference temperature, T_0, and temperature, T, and is given in Table 3.

5.2.2 Visco-Plastic Strain. Inelastic or "viscoplastic" strain includes indistinguishable parts of strain-rate independent plasticity and time-dependant creep. The constitutive equation for glass is obtained from Newtonian incompressible behavior law given in Eq. (16), which relates inelastic strain to stress for glass

$$\sigma = 3\eta(T)\dot{\varepsilon}_{in} \tag{16}$$

where σ is the stress, η is the temperature-dependant viscosity, and $\dot{\varepsilon}_{in}$ is the inelastic strain rate.

The viscosity data were obtained for borosilicate glass [44] and fitted to the following equation [45]:

$$\log \eta = A + \frac{B}{T - T_0} \tag{17}$$

Table 3 Linear coefficient of expansion of steel with temperature, $\alpha(T)$, between reference temperature, T_0 of 20 $^\circ$C and temperature T [27]

Temperature ($^\circ$C)	Expansion coefficient (10^{-6}K^{-1})
200	16
400	17.5
600	18.0
800	18.5
1000	19.5

where $A = 0.5$, $B = 2593$, and $T_0 = 374.8$ are empirical fitting constants.

In Eqs. (16) and (17), when temperature decreases, viscosity increases until it reaches the solidification temperature, T_0. Simple elastic behavior with an initial strain was applied at temperatures below the solidification temperature, where the inelastic strain rate dropped to zero.

5.3   Computational Details. Using an uncoupled approach, the analysis was divided into two parts. In the first part, a thermal analysis was performed to find the temperature field in the domain shown in Fig. 6(a) with boundary conditions in Fig. 6(b). Then this temperature field was incorporated into the thermoviscoplastic stress analysis to calculate the displacement and stresses. Figure 6(c) shows the dimensions, structural boundary conditions, and mesh introduced to the thin slice. The same mesh of axisymmetric four-node heat transfer elements was treated as standard axisymmetric eight-node structural elements in the radial and axial (z) directions for the structural analysis. Vertical displacement, z direction, of all nodes at the top of the slice was coupled, using *EQUATION option in ABAQUS [46]. This approach has been validated with analytical solutions of thermal-stress problems with solidification in previous work [29,47]. It properly allows thermal expansion and contraction of the materials, while enforcing the symmetry constraint that planar sections must remain planar. Contact elements were used in the boundary between the glass and the container in order to simulate the physical interaction between these two parts. No friction data were available for these contacting surfaces, and they were assumed to be frictionless.

The equations for both models were solved using the finite-element method in ABAQUS with a fully implicit stepwise-coupled algorithm for time integration of the governing equations [46]. A set of two ordinary differential equations defined at each material point by the viscoplastic constitutive equations was integrated using the backward-Euler method with a bounded Newton–Raphson method [29] in the user-defined material subroutine user material. Details of the local time integration can be found in Refs. [29,30].

6   Finite-Element Analysis Results

Figure 9 shows a comparison between the thermocouple measurements and predicted finite-element temperature history of thermocouple TC2. During the approximately 10 h filling stage, a peak temperature was observed for each of the two pouring periods. Experimental observations [10] indicated that stresses were generated only during the cooling stage. A simple calculation
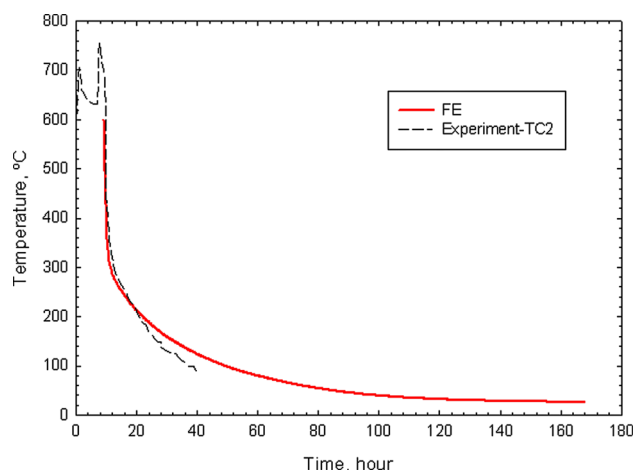
Fig. 9   Comparison between measured and FE predicted steel surface temperature

using the resistor model shown in Fig. 7 indicates that the glass temperature remains above the liquid temperature during the filling stage, so stress cannot develop. Therefore, the model was used only to simulate the cooling process.

The predicted temperature field indicates that the final product cools to the ambient temperature after 160 h (6.6 days). The experimental measured temperature was monitored for only 40 h. An excellent match over 30 h can be seen between the measured temperature and the finite-element prediction.

Figure 10 shows the temperature distribution through the slice inside the glass and stainless steel container. The center of the glass (left) always has a higher temperature than the exterior surface. It can also be seen that the temperature gradient in the glass between the center and surface is greater during the early stages of cooling and drops continuously during the process. For example, this temperature difference is approximately 200 °C after 10 h of cooling and is only 50 °C after 40 h. On the other hand, temperature gradients in the steel are negligible, as its temperature profile is flat. This is due to the high thermal conductivity and small thickness of the steel wall. Figure 10 also shows the effect of the conductance elements acting in the gap between the two parts, which causes a significant temperature drop between the contact surfaces of the glass and stainless steel.

The evolution of the hoop residual stress as a function of time as indicated by the steel casing temperature is shown in Fig. 11 together with the yield stress. It is evident that as the container cools the residual stresses increase until they reach the yield stress at ~200 °C. With further cooling, the residual stress naturally equals the increasing yield stress. Experimental data produced by Pennick [10] showed a similar trend with increasing residual stress with decreasing temperature and essentially reached the tensile yield stress at about 150 °C. The peak hoop stress measured (shown in Fig. 5) using the incremental centre hole drilling method is also illustrated in Fig. 11.

Residual stresses after complete cooling are shown in Figs. 12 and 13. Radial residual stresses in both the glass and steel container are shown in Fig. 12, where the stress distribution is approximately parabolic, dropping from tension in the center to compression in the exterior surface of the glass. The maximum radial tensile stress in the center of the glass is about 4 MPa and interface pressure is about 7 MPa. The steel wall experiences a radial stress gradient dropping from zero gage pressure (ambient) at the surface. The tensile stress in the steel balances the slight net compressive stress found in the glass, so that the entire system is in equilibrium. Hoop residual stresses are shown in Fig. 13. Again, tensile hoop stress generates compressive stress in the glass, especially near the surface. Gradients in hoop stress through the steel are negligible, owing to the thin (5 mm) wall. Experimentally measured peak residual stresses in the wall of the stainless steel are also shown in Fig 13 and match reasonably well.

7   Discussion

In the glass, heat is lost only from its exterior surface through the interface with the stainless steel wall container. Therefore, as seen in Fig. 10, the central part of the glass remains with a higher temperature throughout the whole process. The magnitude and direction of this thermal gradient drives the heat loss. Modeling heat transfer across the gap with a contact resistance function and gap elements was able to realistically represent the conductance [48]. In addition to the temperature dependence included in the model, this thermal contact conductance [48] should increase with pressure across the gap. Neglecting this effect, due to unavailability of data, appears not to cause significant error. Thus, this approach is a reasonable way to account for the imperfections between two rough contacting surfaces. It can be noted in Fig. 10 that the temperature difference between the two contact surfaces is about 600 °C after 1 h. This difference reduces to 500 °C after 10 h of cooling and to only 120 °C after 60 h. The drop in the internal temperature gradients, the drop in temperature difference
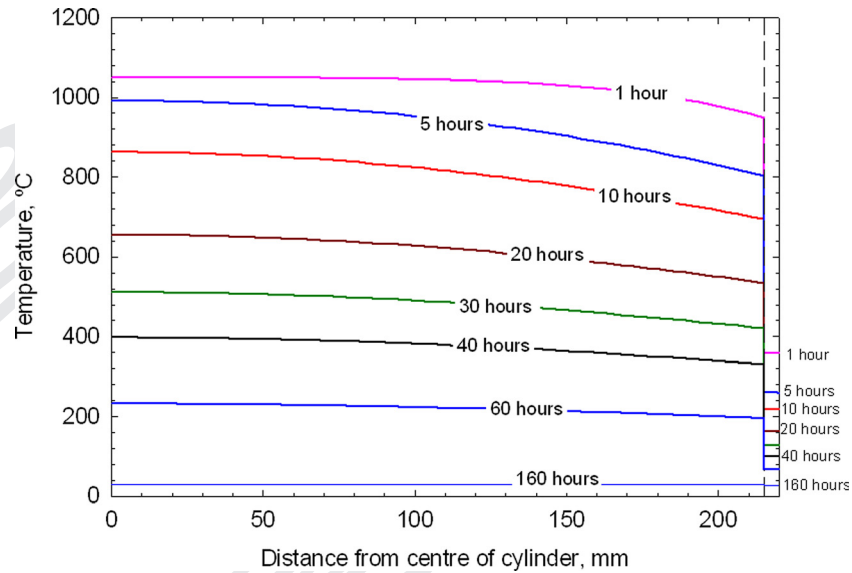
Fig. 10   Predicted temperature distribution through the glass and stainless steel
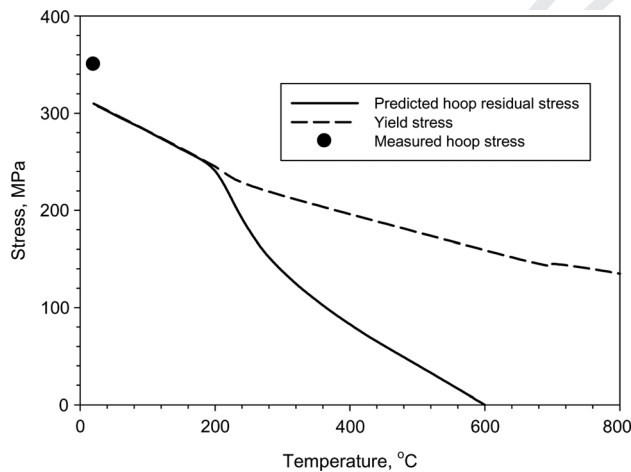

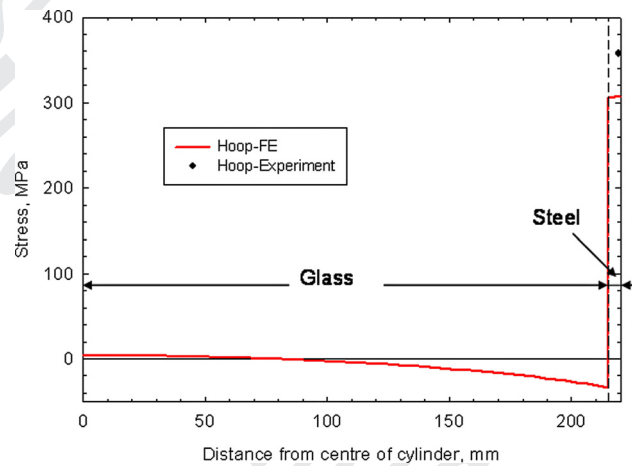Fig. 11   Evolution of residual stress during the solidification process and comparison with yield stress

Fig. 13   Hoop residual stress distribution predicted in the slice compared with experimentally ICHD measurement in middle of steel container wall
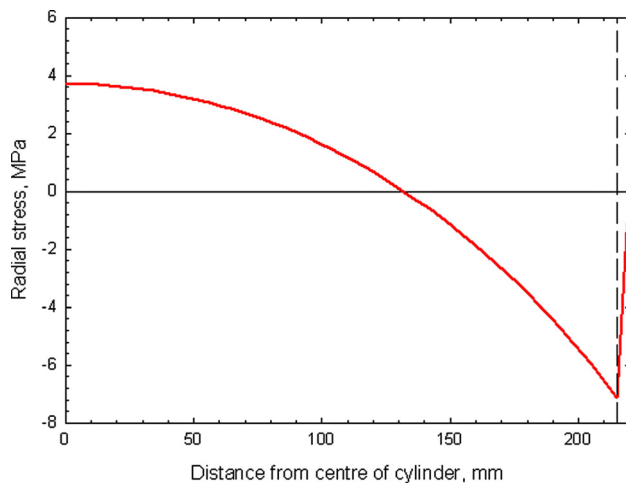
across the gap, and the different properties of glass and steel together are responsible for the development of the residual stresses, which is shown in Fig. 14.

Residual stress inside the glass is generated from both internal thermal stresses and pressure from the steel container wall. The first cause of internal stress in the glass is the changing temperature gradient between the center and the exterior interface, combined with viscoplastic flow. During the cooling process, the exterior surface of the glass cools first, solidifies and contracts around the hot core, which would generally lead to tension in the surface and compression in the center. The compressive stress generated in the hot interior glass quickly relaxes, however, because this glass can flow to accommodate the shrinkage strain, owing to its viscoplastic behavior, which makes it act somewhat like a liquid while it is hot. Later, the temperature gradients relax as the interior cools and contracts within a rigid outer rim. As shown in Fig. 13, after about 60 h this generates a permanent residual stress state of multiaxial tension in the interior, surrounded by compressive membrane stresses in the outer rim to balance. This cooling process is the same phenomenon which occurs during tempering processes that are used to generate compressive residual stresses in the surface of glass plates. Higher cooling rates

Fig. 12   Radial residual stress distribution predicted in the slice
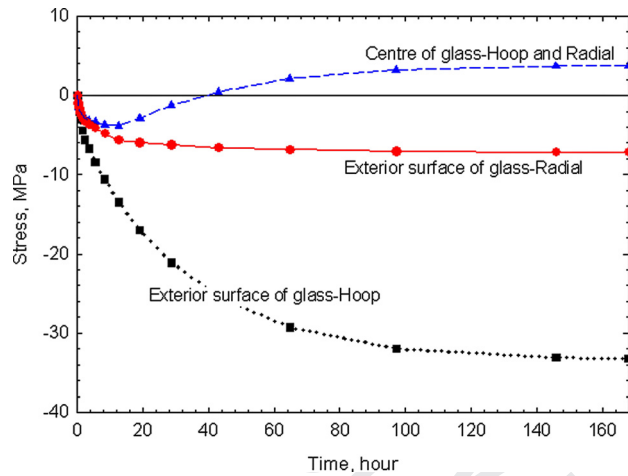
Fig. 14 Stress evolution inside the glass at the central axis and exterior surface (interface with stainless steel)

Fig. 15 Effect of pressure from the container wall on residual stress in glass

in the thermal tempering process lead to steeper temperature gradients, leading to higher residual stresses in tempered glass plates. The tensile residual stresses at the center might lead to cracks and safety problems.

Residual stress in the glass is also affected by the shrinkage of the stainless steel cylinder wall around it. Preheating the steel cylinder causes it to expand prior to filling with the liquid glass. Later, contraction of cooling steel causes pressure against the glass because the thermal expansion coefficient of the steel is larger than that of the glass.

As illustrated in Fig. 12, at the end of cooling stage, the radial pressure of 7.12 MPa is created at the interface of steel and glass. Using an analytical solution for a thin-wall cylinder subjected to an internal pressure, the interface pressure of 7.12 MPa, acts as an internal pressure, so the hoop and axial stresses in the steel can be calculated as

$$\sigma_{\theta\theta} = \frac{pr}{t} = \frac{7.128 \times 210}{5} = 299.4 \, \text{MPa}$$

$$\sigma_{zz} = \frac{pr}{2t} = \frac{7.128 \times 210}{2 \times 5} = 149.7 \, \text{MPa}$$

Comparing between these values, measured residual hoop, and axial stresses in the container, Fig. 5, it appears that the main contribution to the residual stresses generated in the container are due to the internal pressure exerted by the solidified glass. In the axial direction, there is a similar interaction. The stainless steel contracts against the solidified glass and pushes it in the axial direction resulting in axial tensile stress in the wall container and compression axial stress in the glass interface. Therefore, the component of stress from pressure to the top and bottom of the glass will be added to stress component resulted from the internal pressure in the axial direction, 149.7 MPa, to generate the measured axial stress, 280 MPa, shown in Fig. 5.

To investigate the effect of wall pressure on the residual stress, a second simulation was performed with the same temperature history, but using an artificial boundary condition to fix the displacement of the stainless steel wall to prevent it from shrinking. Therefore, stress developed inside the glass without physical interaction with the wall of the stainless steel container. The final hoop stress distribution inside the glass is plotted in Fig. 15 and compared with that of the original model. Without wall pressure, the internal tension becomes higher in order to have average zero stress across the section. Figure 15 thus reveals that the pressure from the wall of the stainless steel pushes the glass, greatly lowering tensile stress at the center of the container and generating more compressive stress near the surface. Because cracks are
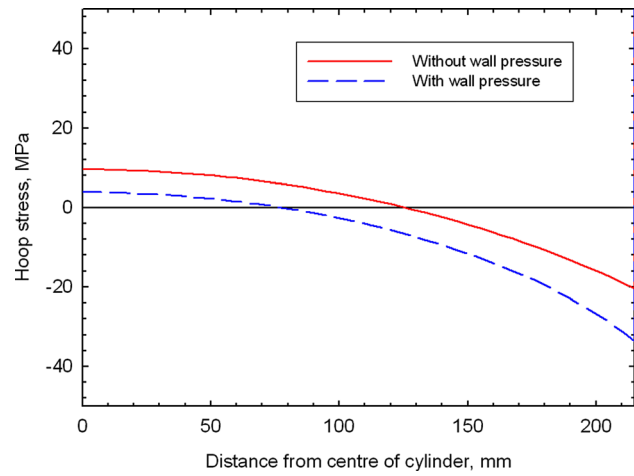
more likely to initiate in the tensile regions, having the wall pressure, probably lowers the chances of crack formation inside the glass. Finally, experimental confirmation of the final residual stress state in the glass remains a significant research challenge.

8 Conclusions

Residual stress measurement and transient finite-element modeling were performed to investigate temperature and stress development in a preheated stainless steel container that is filled with molten glass and allowed to cool. Residual stress measurements reveal the existence of high stresses at the exterior surface of the stainless steel wall container.

The simulation of a representative thin slice through the glass and steel with an elastic-viscoplastic constitutive model of the glass, conducting gap elements, and a generalized plane strain condition reasonably matches measurements of both temperature and stress. This simple but efficient model reveals the process of stress evolution in both the glass and the container. A classic residual stress state of internal tension and surface compression is generated in the glass in a similar manner to the tempering of glass plates. In addition, thermal contraction of the steel container adds additional compression to the glass, which lowers the internal tensile stress levels. This is balanced by tensile stress in the steel wall that causes it to yield.

Nomenclature

$[A], [B]$ = matrices of influence functions for ICHD calculations
  $a(z, h)$ calibration coefficients in a depth of z for a hole with total depth of h
     B = constant parameter
  $b(z, h)$ = calibration coefficients in a depth of z for a hole with total depth of h
    c_p = specific heat (J/kg K)
     D = tensor of elasticity
  $d\text{gap}$ = surface roughness of steel

$E =$ Young's modulus
$H =$ enthalpy
$h$air $=$ film coefficient of air
$k =$ thermal conductivity
$k$eff $=$ effective thermal conductivity
$k$air $=$ thermal conductivity of air
$p, q, t =$ vectors of transformed strains in ICHD
$P, Q, T =$ vectors of transformed stresses in ICHD
$q =$ heat flux
$ra =$ actual incremental center hole drilling gauge radius
$Rm =$ nominal incremental center hole drilling gauge radius
$T =$ temperature
$Tg =$ temperature of steel
$Ts =$ temperature of glass
$Ta =$ temperature of air
$u =$ displacement vector

Greek Letters

$\alpha =$ thermal expansion coefficient
$B =$ orientation of the maximum principle stress in ICHD
$\dot{\varepsilon}_{el} =$ elastic strain rate
$\dot{\varepsilon}_{in} =$ inelastic strain rate
$\epsilon r(\text{h}) =$ relaxed residual strain at the depth h
$\dot{\varepsilon}_{th} =$ thermal strain rate
$\dot{\varepsilon}_{total} =$ total strain rate
$\rho =$ density
$\eta =$ viscosity
$\nu =$ Poisson's ratio
$\Sigma =$ stress
$\dot{\sigma} =$ stress rate
$\sigma_{\max}(z) =$ maximum principal stresses at the depth z
$\sigma_{\min}(z) =$ minimum principal stresses at the depth z

References

[1] Smith, D. J., 2003, "The Influence of Prior Loading on Structural Integrity," Comprehensive Structural Integrity, R. A. Ainsworth, and, K. H. Schwalbe, eds., Elsevier, Amsterdam, Vol. 7, pp. 289–345.
[2] Withers, P. J., 2007, "Residual Stress and Its Role in Failure," Rep. Prog. Phys., 70, p. 2211.
[3] Withers, P. J., and Bhadeshia, H. K. D. H., 2001, "Residual Stress. Part 1-Measurement Techniques," Mater. Sci.Technol., 17, pp. 355–365.
[4] Committee of Radioactive Waste Management, 2006, "Managing Our Radioactive Waste Safely," CoRWM, London, p. 195.
[5] Deokattey, S., Jahagirdar, P. B., Kumar, V., Bhaskar, N., and Kalyane, V. L., 2003, "Borosilicate Glass and Synroc R&D for Radioactive Waste Immobilization: An International Perspective," J. Miner., Met. Mater. Soc., 55, pp. 48–51.
[6] Donald, I. W., Metcalfe, B. L., and Taylor, R. N. J., 1997, The Immobilization of High Level Radioactive Wastes Using Ceramics and Glasses," J. Mater. Sci., 32, pp. 5851–5887.
[7] Hidekazu, A., and Masanori, A., 2005, "Long-Term Integrity of Waste Package Final Closure for Hlw Geological Disposal, (I) Points at Issue Concerning 1,000 Years Containment Capability of Overpack," J. Nucl. Sci. Technol., 42, pp. 470–479.
[8] International Atomic Energy Agency, 2002, "The Long-Term Storage of Radioactivity Waste: Safety and Sustainability," Technical Committee Meetings, IAEA, Vienna, Austria.
[9] Steele, C., 2005, "Aspects of Process Monitoring in the Waste Vitrification Plants (Wvp) at Sellafield," Advances in Process Analytics and Control Technology Conference, Birmingham.
[10] Pennick, A. M., 1987, "Summary of Stress Measurements Made on Glass Containers in the Full Scale Inactive Plant (1984-1986)," BNFL, p. 6.
[11] Andersen, L. F., 2002, "Experimental Method for Residual Stress Evaluation Through the Thickness of a Plate," ASME J. Eng. Mater. Technol., 124, pp. 428–433.
[12] Ficquet, X., Smith, D. J., Truman, C. E., Kingston, E. J., and Dennis, R. J., 2009, "Measurement and Prediction of Residual Stress in a Bead-on-Plate Weld Benchmark Specimen," Int. J. Pressure Vessels Piping, 86, pp. 20–30.
[13] Hossain, S., Truman, C. E., Smith, D. J., and Daymond, M. R., 2006, "Application of Quenching to Create Highly Triaxial Residual Stresses in Type 316h Stainless Steels," Int. J. Mech. Sci., 48, pp. 235–243.
[14] Valente, T., Bartuli, C., Sebastiani, M., and Loreto, A., 2005, "Implementation and Development of the Incremental Hole Drilling Method for the Measurement of Residual Stress in Thermal Spray Coatings," J. Therm. Spray Technol., 14, pp. 462–470.
[15] Nakhodchi, S., Flewitt, P. E. J., and Smith, D. J.,2008, "Stress Measurement in Porous Graphite at Different Length Scales," Securing the Safe Performance of Graphite Reactor Cores, Royal Society of Chemistry, Nottingham, United Kingdom.
[16] Shokrieh, M. M., and Ghasemi K, A. R., 2007, "Determination of Calibration Factors of the Hole Drilling Method for Orthotropic Composites Using an Exact Solution," J. Compos. Mater., 41, pp. 2293–2311.
[17] Schajer, G., and Yang, L., 1994, "Residual-Stress Measurement in Orthotropic Materials Using the Hole-Drilling Method," Exp. Mech., 34, pp. 324–333.
[18] Bathgate, R. G., 1968, "Measurement of Non-Uniform Biaxial Residual Stresss by the Hole Drilling Method," Strain, 4, pp. 20–29.
[19] Mathar, J., 1934, "Determination of Initial Stresses by Measuring the Deformation Around Drilled Holes," Trans. ASME, 56, pp. 249–254.
[20] Rendler, N., and Vigness, I., 1966, "Hole-Drilling Strain-Gage Method of Measuring Residual Stresses," Exp. Mech., 6, pp. 577–586.
[21] Schajer, G. S., 1988, "Measurement of Non-Uniform Residual-Stresses Using the Hole-Drilling Method 1. Stress Calculation Procedures," ASME J. Eng. Mater. Technol., 110, pp. 338–343.
[22] Schajer, G. S., 1981, "Application of Finite Element Calculations to Residual Stress Measurements," ASME J. Mater. Technol., 103, pp. 157–163.
[23] Schajer, G. S., 1998, "Measurement of Non-Uniform Residual Stresses Using the Hole Drilling Method. Part II: Practical Application of the Integral Method," ASME J. Eng. Mater. Technol., 110, pp. 344–350.
[24] Zuccarello, B., 1999, "Optimal Calculation Steps for the Evaluation of Residual Stress by the Incremental Hole-Drilling Method," Exp. Mech., 39, pp. 117–124.
[25] Stefanescu, D., Truman, C., Smith, D., and Whitehead, P., 2006, "Improvements in Residual Stress Measurement by the Incremental Centre Hole Drilling Technique," Exp. Mech., 46, pp. 417–427.
[26] ASTM E 837-01, 2001, "Standard Test Method for Determination Residual Stresses by the Hole Drilling Strain Gauge Method."
[27] Roberts, T., 2004, "The Elevated Temperature Properties of Grade 309 Stainless Steel," BNFL, p. 25.
[28] Koric, S., and Thomas, G. B., 2007, "Thermo-Mechanical Model of Solidification Processes With ABAQUS," ABAQUS Users Conference, Paris, France, pp. 320–336.
[29] Koric, S., and Thomas, B. G., 2006, "Efficient Thermo-Mechanical Model for Solidification Processes," Int. J. Numer. Methods Eng., 66, pp. 1955–1989.
[30] Koric, S., Hibbeler, L. C., and Thomas, G. B., 2009, "Explicit Coupled Thermo-Mechanical Finite Element Model of Steel Solidification," Int. J. Numer. Methods Eng., 78, pp. 1–31.
[31] Zhu, H., 1993, "Coupled Thermal–Mechanical Finite-Element Model With Application to Initial Solidification," Ph.D. thesis, Department of Mechanical and Industrial Engineering, University of Illinois, Urbana, USA.
[32] Li, C., and Thomas, B. G., 2005, "Thermo-Mechanical Finite-Element Model of Shell Behavior in Continuous Casting of Steel," Metall. Mater. Trans. B, 35, pp. 1151–1172.
[33] Budinski, K. G., and Budinski, M. K., Engineering Materials Properties and Selection (Prentice Hall, ■, 2005).
[34] Aben, H., and Guillemet, C., Photoelasticity of Glass (Springer-Verlag, ■,1993).
[35] Carre, H., and Daudeville, L., 1996, "Numerical Simulation of Soda-Lime Silicate Glass Tempering," J. Phys. IV France 06 C1-175-C171-185.
[36] Indenbom, V. L., 1954, "A Theory of Glass Annealing," Zhurnal Sakharnoi Promyshlennosti, 24, pp. 925–928.
[37] Narayanaswamy, O. S., 1978, "Stress and Structural Relaxation in Tempering Glass," J. Am. Ceram. Soc., 61, pp. 146–152.
[38] Parsa, M. H., Rad, M., Shahhosseini, M. R., and Shahhosseini, M. H., 2005, "Simulation of Windscreen Bending Using Viscoplastic Formulation," J. Mater. Process. Technol., 170, pp. 298–303.
[39] Moreau, P., Locheginies, D., and Oudin, J., 1998, "An Inverse Method for Prediction of the Required Temperature Distribution in the Creep Forming Process," Proc. Inst. Mech. Eng., Part E: J. Process Mech. Eng., 212, pp. 7–11.
[40] Locheginies, D., Moreau, P., and Oudinn, J., 1996, "Finte Element Strategy for Glass Sheet Manufacture by Creep Forming," Commun. Numer. Methods Eng., 12, pp. 331–341.
[41] Park, J. K., Thomas, B. G., and Samarasekera, I. V., 2002, "Analysis of Thermomechanical Behaviour in Billet Casting With Different Mould Corner Radii," Ironmaking Steelmaking, 29, pp. 359–375.
[42] Thomas, B., Samarasekera, I., and Brimacombe, J., 1987, "Mathematical Model of the Thermal Processing of Steel Ingots: Part I. Heat Flow Model," Metall. Mater. Trans. B, 18, pp. 119–130.
[43] Thomas, B. G., 1995, "Issues in Thermal–Mechanical Modeling of Casting Processes," ISIJ Int., 35, pp. 737–743.
[44] Anurag, J., Gregory, C. F., and Allen, Y. Y., 2005, "Viscosity Measurement by Cylindrical Compression for Numerical Modeling of Precision Lens Molding Process," J. Am. Ceram. Soc., 88, pp. 2409–2414.
[45] Fulcher, G. S., 1925, "Analysis of Recent Measurement of the Viscosity of Glasses," J. Am. Ceram. Soc., 8, pp. 339–355.
[46] Dassault Crop., 2008, "abaqus User Manuals," abaqus, Inc., Pawtucket, RI.
[47] AydIner, C. C., and Üstündag, E., 2005, "Residual Stresses in a Bulk Metallic Glass Cylinder Induced by Thermal Tempering," Mech. Mater., 37, pp. 201–212.
[48] Yu ncu, H., 2006, "Thermal Contact Conductance of Nominally Flat Surfaces," ASME Heat Mass Transfer, 43, pp. 1–5

AQ4

AQ1: Please provide the postal code for this affiliation.

AQ2: Please provide the state name for this present address.

AQ3: Please check whether "in the next section" refers to Sec. 4 in the sentence beginning with "These are presented…"

AQ4: Please provide the publisher's location for Refs. 33 and 34.